Verification of effect of interference between multiple scatterers on the evaluation of backscattering coefficient

Hayato Kutsuzawa, Shinnosuke Hirata, Kenji Yoshida, Emilie Franceschini, Tadashi Yamaguchi

Verification of effect of interference between multiple scatterers on the evaluation of backscattering coefficient

Hayato Kutsuzawa[1]*, Shinnosuke Hirata[2], Kenji Yoshida[2], Emilie Franceschini[3], Tadashi Yamaguchi[2]**

[1] *Graduate School of Science and Engineering, Chiba University, Yayoicho, Inage, Chiba 263-8522, Japan*

[2] *Center for Frontier Medical Engineering, Chiba University, Yayoicho, Inage, Chiba 263-8522, Japan*

[3] *Aix-Marseille University, CNRS, Centrale Marseille, LMA, Marseille 13013, France*

E-mail: h_kutsuzawa@chiba-u.jp*, yamaguchi@faculty.chiba-u.jp**

Abstract

Backscattering coefficient (BSC) analysis methods for biological tissues have been clinically applied, but they are based on the theory of a homogeneous scattering medium. In this paper, the effect of spatial correlation of waves between scatterers on the backscattering properties of inhomogeneous mediums containing two types of scattering sources with different acoustic properties was investigated. In the echo data of a phantoms containing two types of scatterers acquired by multiple sensors, the power and frequency dependence of the BSC were different from theoretical calculations due to the interference effects of each scatterer. The effect of interference between the two types of scatterers was confirmed to be particularly strong for echoes acquired by the sensor at high intensity and high frequency, or for higher number densities of strong scatterers.

1. Introduction

Quantitative ultrasound (QUS) is useful for noninvasive evaluation of diseases of various biological tissues such as liver, breast, lymph nodes, skin, and bone. In particular, amplitude envelope statistics,[1-6] attenuation coefficients (AC),[7-10] backscatter coefficients (BSC),[11-15] and elastography[16-21] have attracted attention in clinical practice, and tools for evaluating QUS parameters which were obtained from these techniques have been implemented in clinical ultrasound systems.

Since backscatter coefficient depends on physical quantities such as the scatterer diameter, volume fraction, and acoustic impedance ratio of the scatterer and surrounding medium, the physical quantity to be evaluated can be estimated by comparing the measured backscatter coefficient with a theoretical model.[22,23] It has been reported that evaluation of fatty liver,[24,25] dermal lymphedema,[26-28] thyroid tumors,[29,30] and trabecular bone[31] is possible using the backscatter coefficient as an indicator. BSC evaluations using single-element concave transducers have been widely used in these basic studies.

There are also reports of evaluation using multiple frequency bands,[32,33] plane wave compound imaging,[34-36] and spatial synthesis[11,13] to improve evaluation accuracy. Omura et al. used multiple ultrasound scanners to acquire signals with two different beamforming methods, line-by-line beamforming with focused imaging and parallel beamforming with plane-wave imaging, and verified the variation of BSC.[36] The calculated BSC was independent of either the system setting or the beamforming method, and the feasibility of BSC analysis using plane wave imaging was demonstrated.

However, the accuracy of quantitative evaluation is limited even when plane waves are also used, because multiple types of scattering sources are mixed in biological tissues. There is a trend to consider the influence of structures in the tissue and interference between scatterers as the main causes of this problem. Scattering sources in biological tissue are densely intermingled, with multiple sources within the point spread function (PSF) of the transducer. Therefore, backscatter characterization is usually based on the speckle signal, which is the interference between the scatterers. In other words, it is necessary to understand the spatial correlation between scatterers. The effect of spatial correlation in a homogeneously distributed medium with one type of scatterer is well understood. E. Franceschini et al. investigated a scattering model from the perspective of explaining experimental BSCs from cell pellet biophantoms with a single structural and acoustic parameter set.[37] They reported that the impedance and size estimated from the scattering model were satisfactory. On the other hand, spatial correlations between scatterers in

heterogeneous media containing a mixture of scatterers with different acoustic properties have not been well studied. Therefore, the interpretation of backscatter coefficients from complex biological tissues first requires an understanding of ultrasonic backscatter from a biological phantom with known scattering conditions, especially the effects of wave interference caused by the positional correlation of scatterers.

In this study, we focused on the effect of interference between scatterers and compared the backscatter coefficients of phantoms with two different types of scatterers at different scattering ratios. Using a self-made ultrasonic scanner and a single concave transducer, the backscatter coefficients at low and high frequencies were evaluated. We also evaluated them using a research platform scanner and a very high-frequency linear array probe. In particular, signals were acquired using the parallel beamforming method with plane wave imaging and BSC analysis was performed.

2. Materials and Methods

2.1 Tissue-mimicking phantoms of multiple types of scatterers

Seven different rectangular phantoms (8 cm in width × 2 cm in length × 4 cm in height) were prepared as reference and evaluate phantoms. The solvents of each phantom were 2 wt% agar (A1296; Sigma-Aldrich, MO, USA) and distilled water. The weak scatterers were nylon spheres with an average particle size of 5 μm (ORGASOL 2001 EXD NAT 1; Arkema, Colombes, France), and the strong scatterers were acrylic spheres with an average particle size of 20 μm (MX-2000; Soken, Aichi, Japan). The intrinsic acoustic impedances are 1.493 and 1.665 Mrayl, respectively. These scatterers were mixed at various volume fractions as shown in Table I.

Phantom A and B are homogeneous media with only one type of scatterer. They were created as reference medium which the spatial correlations between scatterers are known for comparison with phantoms which contain two types of scatterers. Phantom A was created so that the scattering intensity was equivalent to that of a normal liver. Phantom B is a case in which only fat droplets are present, which is not possible in actual living tissue. Phantoms C, D, and E are groups in which fat droplets (strong scatterers) are mixed in different fractions within the normal liver (weak scatterers),[38] while phantoms D, F, and G are groups in which fat droplets are constant and liver components are different fractions. By comparing the BSCs of these phantoms, the fraction (distribution) of the two types of scatterers and the effects of scattering and mutual interference from each scatterer can be evaluated.

2.2 Data acquisition using the laboratory-made scanner

Three-dimensional RF echo signals were observed using a laboratory-made ultrasonic scanner and two types of single-element concave transducers [transducer I (V327; Olympus, Tokyo, Japan) and transducer Ⅱ (PT35; TORAY, Tokyo, Japan)]. The center frequency and -6 dB bandwidth are 10 MHz ± 3 MHz and 30 MHz ± 10 MHz, respectively. The depth of focus and f-number are 19.7 mm, 10mm, and 2.10, 1.85, respectively. For echo data acquisition, pulser receiver I (Model 5800; Olympus, Tokyo, Japan) for V327 and pulser receiver Ⅱ (DPR500; JSR Ultrasonics, NY, USA) for PT35] for PT32 were used to excite negative impulses to the element for transmission. After the echo signals were received, they were band-pass filtered at 1-35 MHz and 30-300 MHz, respectively, by the receiver circuit in each pulser receiver. Each echo signal was quantized at 12-bits by the oscilloscope (HDO6104; Teledyne LeCroy, NY, USA) set to the sampling frequency of 250 MHz. The PSF near the focus of each transducer is shown in Table II. The transducer was fixed to a triaxial linear rail (MTN100CC, Newport) and mechanically scanned in the lateral and slice directions. The phantom was fixed in degassed water at 22-24°C. Echo signals were acquired by irradiating ultrasound from the top surface. The depth of field of each transducer was 17.8-21.5 mm for V327 and 9.7-10.7 mm for PT35, so the phantom surfaces were set to 17 mm and 9 mm, respectively, in order to cover the analysis area within the depth of field. The scan pitch was 30 μm in both lateral and slice directions. Three-dimensional RF echo signals of 4096 in depth × 501 in latetal × 101 in slice pixels were acquired for all phantoms. All data acquisition and motor stage control were controlled by LabVIEW (National Instruments, TX, USA).

2.3 Data acquisition using the research-platform scanner

Two-dimensional RF echo signals were acquired using the research-platform scanner (Vantage256; Verasonics, WA, USA) and a linear array probe (L39-21gD; Verasonics, WA, USA). The center frequency and -6 dB bandwidth were 25 MHz ± 9 MHz. The element pitch and the number of elements were 0.055 mm 128 channels, respectively. The focus depth in the elevation direction was approximately 6.5 mm. Each echo signal was quantized at 14-bits with the sampling frequency set to 4/3 times the center frequency. In addition, the acquired data were up-sampled by a factor of 3 in the depth direction to produce data with a sampling frequency that is effectively 4 times the center frequency. The PSF at the highest resolution point is shown in Table II. RF data of each B-mode plane of each

phantom were acquired by plane wave imaging with parallel beamforming. Plane waves were steered at 11 angles (0°, ±1°, ±2°, ±3°, ±4°, and ±5°), and the analysis signal was generated by combining them after delay and sum (DAS).

2.4 Speed of sound and attenuation coefficient calculation

The speed of sound and the attenuation of each phantom were evaluated by the reflection method before BSC analysis. 3-D RF echo signals were acquired using a single-element plane transducer III (V312; Olympus, Tokyo, Japan) in the same setting as transducer I in 2.2. The center frequency and -6 dB frequency bandwidth are 10 MHz ± 3 MHz. Echo signals were also acquired using transducer II under similar conditions. An acrylic plate was placed on top of the sound absorber, and the echo signals were acquired with and without the sample while maintaining the positional relationship between the transducer and the acrylic plate.[39] The transducer was set at the depth at which the signal from the acrylic plate was maximum. The speed of sound was calculated from the time of flight (TOF) based on the time difference between the maximum amplitude returned from the sample and the acrylic plate as follows:

$$c_p = c_0 \left(1 + \frac{t_{ref} - t_r}{t_b - t_s}\right), \tag{1}$$

where t_s is the TOF from the sample surface, t_b is the TOF from the back, t_r is the TOF from the acrylic plate after the sample passed through, and t_{ref} is the TOF from the acrylic plate at the same position as during the measurement. c_0 is the speed of sound of water. The thickness d of the sample was calculated by $d = c_0(t_b - t_s)/2$. The attenuation rate of the phantom, α [dB/cm], was calculated using the power spectra with and without the sample as follows:

$$\alpha(d, f) = \frac{8.686}{4d} \ln \frac{P_s}{P_{ref}}, \tag{2}$$

where P_s is the power spectrum through the phantom and P_{ref} is the power spectrum without the sample. α is the total attenuation at an arbitrary frequency f. The attenuation rate can be considered to be the same as the absorption rate when the frequency is somewhat low, when absorption attenuation can be considered to be dominant, or when scattering is ignorable in a relatively homogeneous medium. In particular, in the frequency band between 1 MHz and 10 MHz used in clinical used ultrasonic diagnostic equipment, it can often be approximated as proportional to the first power of the frequency. Therefore, the attenuation coefficient α_0 [dB/cm/MHz] can be written as $\alpha(f) = \alpha_0 f + b$. On the other hand, the

frequency dependence of attenuation is considered to be an important characteristic in the frequency band above 10 MHz, and the dependence of attenuation on frequency is described as $\alpha(f) = \alpha_0 f^n + b$, where n as well as α_0 is considered to vary.[40] Therefore, the parameters when approximated by the equations $\alpha(f) = \alpha_0 f + b$ and $\alpha(f) = \alpha_0 f^n + b$ were calculated for the signals measured with transducer III and transducer II, respectively, using the least-squares method with a -6 dB bandwidth.

2.5 Backscatter coefficient analysis using reference phantom method

Backscatter coefficient was calculated using the reference phantom method.[41] The reference phantom method assumes that the attenuation properties and backscatter coefficient of the phantom used as the reference medium and the attenuation properties of the analysis medium are known. By using a medium with known scattering conditions as a reference signal, the backscatter coefficient can be evaluated robustly by correcting the sound field of the transmitting and receiving systems when evaluating a medium with complex beam diffraction effects such as a linear array probe or a medium with complex scatterer structures such as biological tissue. The array probe can be used to evaluate backscatter coefficient with high robustness. For this reason, array probes are widely used. In this study, a region of interest (ROI) was set up to analyze local RF signal characteristics, and the backscatter coefficient for each ROI was estimated. The ROI size was 10 times the wavelength at the center frequency of the transducer in the depth direction and 10 uncorrelated echo lines in the lateral direction. Backscatter coefficient was estimated as

$$BSC(f) = \frac{\overline{P(f)}}{\overline{P_r(f)}} BSC_r(f) \exp\left\{\frac{4(\alpha - \alpha_{ref}) f \left(x_0 + \frac{\Delta z}{2}\right)}{8.686}\right\} \quad (3)$$

where $\overline{P(f)}$ represents the average of the power spectrum of the analyte in the ROI and $\overline{P_r(f)}$ represents the power spectrum of the reference medium. The frequency response of the measured echo signal includes a component of attenuation that occurs during ultrasonic wave propagation. Therefore, the last section corrects for the attenuation up to the analysis window. α and α_{ref} are attenuation coefficients, x_0 is the distance from the scattering medium surface to the start of the analysis window, and Δz is the size of the analysis window.[42]

In the frequency range from 1 MHz to 10 MHz, $n = 1$, since the attenuation can be assumed to be proportional to the power of one of the frequencies. $BSC_r(f)$ is the theoretical value of the backscatter coefficient of the reference medium. In this study, the

reference phantom was evaluated as Phantom A. The theoretical values were calculated by the mathematical model as follows:

$$BSC_r = m\int_0^\infty p(r)\sigma_{b\_\mathrm{elastic}}(k,r,\gamma)S(k,r,\varphi)dr, \quad (4)$$

where m is the number density of scatterers. $p(r)$ is the probability density function of scatterers, which can be assumed by performing calculations for each scatterer diameter when there is a distribution of scatterer diameters and finally performing weighted integrals. $\sigma_{b\_\mathrm{elastic}}(k,r,\gamma)$ is the Faran model[43], which assumes that the scatterers are elastic and transverse waves propagate. It assumes that the scattering body is elastic and shear waves propagate. $S(k,r,\varphi)$ is the structure factor and assumes that the scatterer is dense and the randomness of the scatterer's position is impaired. r, k, γ and φ are the particle size, wavenumber, acoustic impedance ratio, and volume fraction of the scatterer, respectively.

In order to verify the effect of interference between the two types of scatterers, the deviation between the evaluated backscatter coefficient and the theoretical value of the backscatter coefficient was calculated. The theoretical value of the backscatter coefficient was calculated in the same way as in equation (4). The average deviation was defined as

$$\mathrm{Deviation} = \frac{1}{\mathrm{BW}}\sum_{f\ \mathrm{in\ BW}}\{BSC(f) - BSC_{ref}(f)\}, \quad (5)$$

where BW indicates the frequency band used in the analysis.

3. Results

3.1 BSC evaluation of phantoms with one type of scatterer

To understand the characteristics of the phantoms used for reference, phantom A and B which contain only one type of scatterer were measured with three single-element concave transducers and linear probe. B-mode images of phantom A and B acquired using transducer I, transducer II, and the linear array probe are shown in Fig. 1. Each B-mode image was normalized by the maximum value of phantom B. Because the acoustic impedance of scatterer 2 is higher than that of scatterer 1, the amplitude of phantom B is larger in each transducer.

In phantom A, the number of scatterers present is 749, 28.9, and 88 relative to the PSFs of the transducer I, transducer II, and linear array probe, respectively, which is confirmed to be speckle (Fig. 1(a-1)-(c-1)).

In phantom B, on the other hand, the number of scatterers present is 7.02, 0.27, and 0.82, respectively, so that scatters acquired with transducer I are speckles, while those

acquired with transducer II and the linear array probe can be identified as point sources (Fig. 2(a-2)-(c-2)).

The amplitude envelopes of phantom A and B acquired by each sensor are shown in Fig. 2. The F-values of transducers I and II are 2.10 and 1.85, respectively, and the sound pressure gradient of transducer II is steep. Therefore, the signal below 12 mm is equivalent to the amplitude value in the water region, and the S/N ratio is not sufficiently high (Fig. 2(b)). On the other hand, the data measured by the linear array probe shows a high signal intensity, and a high S/N ratio is guaranteed even in deep areas (Fig. 2(c)).

The frequency spectrum of phantom A and B acquired by each sensor are shown in Fig. 3. Each frequency spectrum is normalized by the maximum value of each phantom. Transducer I has a narrow effective bandwidth (Fig. 3(a)), while transducers II and linear array probes have a wide effective frequency band in the very high frequency range (Fig. 3 (b), (c)).

The results of the backscatter coefficient estimation for phantom A and B using each single-element transducer and their respective theoretical values are shown in Fig. 4. Phantom A is self-referencing, so the sound field and attenuation corrections can be performed with high accuracy, and the results are in agreement with theoretical values. For Phantom B, the results for transducer I agreed with the theoretical values, confirming the high precision of the evaluation (Fig. 4(a)). However, in the high-frequency band, there was no complex frequency dependence as in the theoretical values, and the deviation was large. (Fig. 4(b), (c)).

3.2 BSC evaluation of phantoms with two types of scatterers

3.2.1 Effects of increasing strong scatterers

Based on the trend of the backscatter coefficient evaluation results for phantoms with only one type of scatterer mixed in, the effect of the number density of strong scatterers on the backscattering characteristics was confirmed. B-mode images of phantom C, D, and E acquired using transducer I, transducer II, and linear array probe are shown in Fig. 5. Normalization method of B-mode images was the same as in Fig. 1(a-2)-(c-2). Comparing phantom C, D, and E in transducer I, the amplitude increases as the scatterer number density increases (Fig. 5(a)). In transducer II, the amplitude did not change as the number density increased (Fig. 5(b)). On the other hand, in the linear array probe, the amplitude of the phantom decreases as the number density increases. In particular, strong scatterers are recognizable as point sources, and the amplitude of strong scatterers decreases gradually

(Fig.5(c)).

The amplitude envelopes of phantom A, B, C, D, and E in each sensor are shown in Fig. 6. For comparison, Figure 6 also presents results for phantom A and B. Since the signal intensity from the surface waves is similar for both phantoms, it can be assumed that the intensity of the incident ultrasound signal of the phantoms in this study is similar (Fig. 6 (a), (b)). This is because the number density of scatterers in the phantom in this study is sufficiently small, and the reflected wave signal from the phantom surface does not include the reflected wave from the scatterers, but is considered to be the reflection from the surrounding medium, the agar phantom. In the amplitudes acquired by the linear array probe, the scatterer number density increases in the order of phantom B, D, and E, but the amplitudes are lower in the order of phantom B, D, and E (Fig. 6 (c)).

The frequency spectrums of phantom A, B, C, D, and E observed with transducer I, II, linear array probe are shown in Fig. 7. The power was normalized by the maximum value of each phantom. The bandwidth widens as the scatterer number density increases in transducer I. Both phantoms were speckle signals, and the total power of the signal increased as the number density increased (Fig. 7 (a)). In transducer II and the linear array probe, the bandwidth is narrower than in phantom A because the signal from the strong scatterer is acquired as a point scattering source. In phantom C and D and E, the higher number density of scatterers in the PSF increases the signal at lower frequencies, while the signal at higher frequencies decreases due to greater scattering attenuation (Fig. 7 (b), (c)).

The estimated and theoretical backscatter coefficients for phantom C, D, and E at each transducer are shown in Fig. 8. The theoretical value of the two-scatterer mixed phantom is the value obtained by substituting the probability density function of the scatterer particle size for each phantom into the probability density function in eq. 5. In other words, it is the sum of the theoretical values of the backscattering coefficients of each scatterer. That is, it is the sum of the theoretical values of the backscattering coefficients of each scatterer. Thus, interference between each scatterer is taken into account, but the effect of mutual interference between the two types of scatterers is not taken into account. There was no difference in the frequency dependence of each phantom in transducer I. As the number of strong scatterers increases, the value of the backscatter coefficient is higher, and the values for phantom C and D are consistent with the theoretical values (Fig. 8 (a)). In transducer II, the estimation results are similar for the phantom with two mixed scatterers, as in phantom B, with a large deviation from the theoretical value. In particular, the properties of phantom D are strongly consistent with phantom B (Fig. 8 (b)).[38] The results of the evaluation with

the linear array probe show a lower value compared to Phantom B, although the deviation from the theoretical value is large. Comparing phantom C, D, and E, the backscatter coefficients show lower values as the scatterer number density increases (Fig. 8 (c)).

The deviation between the estimated backscatter coefficient and the theoretical value calculated by the mathematical model is shown in Fig. 9. Although Phantom B has only one type of scatterer, the deviation from the theoretical value is so large that it is difficult to compare with the deviation calculated by eq. 7. Therefore, the deviations of the other phantoms were normalized at each frequency so that the deviation of phantom B was zero, and the mean and standard deviation were calculated. The theoretical value of the backscatter coefficient is a model that does not take into account the interference between the two types of scatterers, whereas the measured evaluation results include their effects, and the deviation indicates the degree of such interference. A smaller standard deviation indicates a smaller frequency-dependent deviation. Since the evaluation of phantom A is self-referencing and the evaluation is highly accurate in all modalities, the deviation of phantom A is not calculated. The mean and standard deviation of the deviation in transducer I are within 3 dB, indicating a high degree of agreement with the theoretical values. The mean deviation for transducer II and the linear array probe was lower with increasing scatterer number density, and the standard deviation of the deviation was larger for the linear array probe.

3.2.2 Effects of increasing weak scatterers

To confirm the effect of increasing of week scatterers, phantom D, F, and G were compared. B-mode images of phantom D, F, and G acquired using transducer I, II, and the linear array probe are shown in Fig. 10. Normalization method of B-mode images was the same as in Fig. 1(a-2)-(c-2). In Fig. 10, it is confirmed the amplitudes of transducer I are similar for an increasing number of weak scattering sources (Fig. 10(a)). B-mode images acquired with the transducer II and linear array probes show a low-contrast image with a small amplitude of the strong scattering source as the weak scatterer increases (Fig. 10(b), (c)).

The amplitude envelopes of phantom D, F, and G using transducer I, transducer II, and linear array probes are shown in Fig. 11. The amplitude envelopes of phantom A and B are also shown for comparison. The similarity of phantom B, D, and F in the signals acquired with transducer I indicates that the strong scatterer is dominant in the reflected signal. Phantom G has a sufficiently high number density of weak scatterers, and many scatterers are mixed in near the phantom surface. Because the reflected waves from the scatterers are

included in the surface wave signal of the phantom, the surface waves are larger than those of other phantoms and the signal inside the phantom is also lower (Fig. 11(a)). The signal intensities of phantom B, D, F, and G acquired with transducer II are comparable, and the amplitude gradient of the signal below the focus is steeper as the number density increases due to scattering attenuation (Fig. 11(b)). Signals acquired with the linear array probe show an increase in scatterer number density but lower amplitude when compared to phantom B, D, and F. Phantom G is difficult to compare with other phantoms, because the intensity of the incident signal is smaller than the other phantoms due to the larger surface waves in Fig. 11(a). However, comparison of phantom B, D, and F suggests that the scattering intensities are not simply additive (Fig. 11(c)).

The frequency spectrums of phantom A, B, D, F, and G acquired using each sensor are shown in Fig. 12. For transducer I, the frequency bandwidth tended to narrow as the number of weak scatterers increased (Fig. 12(a)). For the transducer II and linear array probes, as in Fig. 7(b),(c), the low-frequency signal increased with each increase in scatterer number density, but the high-frequency signal decreased due to high-frequency attenuation (Fig. 12(b),(c)).

The estimated backscatter coefficients of phantom D, F, and G acquired by each sensor and the theoretical values calculated by the mathematical model are shown in Fig. 13. The theoretical values for a phantom with two mixed scatterers are calculated in the same way as in chapter 3.2.1. Phantom B, D, F and G were similar in transducer I (Fig. 13(a)). The deviation from the theoretical value was large for transducer II, while results for B, D, and F were similar. On the other hand, phantom G shows lower values than the other phantoms, and the difference is larger than the difference between the theoretical values (Fig. 13(b)). In the linear array probe, as in transducer II, the deviation from the theoretical value is large but low as the scatterer number density increases. The frequency dependence is also different in the frequency range from 25 MHz to 35 MHz, where the slope becomes smaller as the number density increases (Fig. 13(c)).

The deviation between the estimated backscatter coefficient and the theoretical value calculated by the mathematical model is shown in Fig. 14. The same as in Fig. 9, normalized by Phantom II. For all modalities, the mean value of the deviation was higher as the scatterer number density increased. In addition, the standard deviations of the deviations are larger for transducer I, transducer II, and the linear array probe, in that order.

4. Discussion

In this study, the effect of the interference state between different scatterers on the backscattering characteristics was examined by changing the ratio of the scatterers in a medium with multiple types of scatterers. The amplitudes were evaluated for the medium with a fixed amount of weak scatterers and an increased amount of strong scatterers, and for the medium with a fixed amount of strong scatterers and an increased amount of weak scatterers, as shown in Figs. 5(c) and 10(c). The amplitude is low even in shallow areas as the number density increases due to the weaker interference caused by the mixture of two types of scatterers. As shown in Fig. 5(a) and Fig. 10(a), the intensity of the surface wave does not change between phantoms, indicating that it is not due to the reflection of the surface wave.

As shown in Fig. 8(a) and Fig. 13(a), the theoretical model for a phantom with two types of scatterers does not consider the interference between the two types of scatterers. Therefore, the mutual influence between the two types of scatterers is small in the theoretical value. On the other hand, in the actual measurements, as shown in Figs. 8(b) and 13(b), the scattering from the strong scatterer is sufficiently larger than that from the weak scatterer, and the signal from the strong scatterer is dominant in the two-scatterer mixed phantom. Therefore, the interference signal between the weak scatterers is small, and it is assumed that the backscattering coefficient is estimated low in Figure 8(c) because the strong scatterers in the analysis region are weakened by the interference with the surrounding weak scatterers and the contrast is reduced. This can be understood from the fact that the slope as well as the power is smaller, as shown in Fig. 13(c). In other words, it is due to the effect of weaker interference from strong scatterers and more dominant signals from weak scatterers.

As shown in Fig. 9 and Fig. 14, the standard deviation of the deviation is larger for each increase in the number density of scatterers in the order of transducer I, transducer II, and the linear array probe, and the data acquired with the linear array probe shows the largest deviation from the frequency dependence, indicating the influence of interference. The deviation in transducer II shows the difference between the theoretical values and is not due to the effect of interference, because the difference between the phantoms in the backscatter coefficient evaluation results is small as shown in Fig. 8(b) and Fig. 13(b). The standard deviation of the deviation in transducer I is small, indicating that the frequency dependence of the deviation is highly consistent despite the difference in power. Thus, interference between the two types of scatterers has a significant effect on the backscattering characteristics when evaluated with a high intensity and high frequency sensor.

5. Conclusions

In order to understand the influence of wave interference caused by the correlation of scatterer positions, we compared the backscattering characteristics of a phantom with a mixture of two types of scatterers when the ratio of the scatterers was changed, using several sensors. The signal acquired with a single transducer showed only a small influence of interference, while the signal acquired with a linear array probe of high intensity and high frequency showed a weaker influence of interference, which became more pronounced as the number density of scatterers increased. However, the scattering intensity of actual biological tissue differs significantly from that of the simulated biological samples used in this study and has a more complex scatterer distribution, so the frequency dependence of the BSC is also assumed to have more diverse variations. In future works, we will evaluate the scattering intensity of real biological tissue as well as media with heterogeneous scatterer distribution and structure, which are closer to the scattering intensity of biological tissue.

Acknowledgments

This work was partly supported by JSPS KAKENHI Grant Number 23H03758, and Chiba University Institute for Advanced Academic Research.

References

1) T. Yamaguchi, H. Hachiya, J. Med. Ultrason. **37** [4], 155 (2010).
2) S. Mori, S. Hirata, T. Yamaguchi, and H. Hachiya, Jpn. J. Appl. Phys. **57,** 07LF17 (2018).
3) K. Tamura, J. Mamou, K. Yoshida, H. Hachiya, and T. Yamaguchi, Jpn. J. Appl. Phys. **59**, SKKE23 (2020).
4) M. Omura, K. Yoshida, S. Akita, and T. Yamaguchi, Jpn. J. Appl. Phys. **57**, 07LF15 (2018).
5) Y. Sato, K. Tamura, S. Mori, D. Tai, P. Tsui, K. Yoshida, S. Hirata, H. Maruyama, and T. Yamaguchi, Jpn. J. Appl. Phys. **60**, SDDE06 (2021).
6) Y. Ujihara, K. Tamura, S. Mori, S. Hirata, K. Yoshida, H. Maruyama, and T. Yamaguchi, Jpn. J. Appl. Phys. **62**, SJ1043 (2023).
7) Y. Koizumi, M. Hirooka, N. Tamaki, N Yada, O. Nakashima, M. Kudo, and Y. Hiasa, **14** [8], 1 (2018).
8) Y. Fujiwara, H. Kuroda, T. Abe, K. Ishida, T. Oguri, S. Noguchi, T. Sugai, N. Kamiyama, and Y. Takikawa, Ultrasound Med. Biol. **44** [11], 2223 (2018).
9) Y. Fujiwara, H. Kuroda, T. Abe, K. Ishida, T. Oguri, S. Noguchi, T. Sugai, N. Kamiyama, and Y. Takikawa, Ultrasound Med. Biol. **44** [11], 2223 (2018).
10) S. Kyung, I. Joo, S. Y. Kim, J. K. Jang, J. Park, H. S. Park, E. S. Lee, and J. M. Lee, Ultrasonography **40** [1], 136 (2021).
11) W. Saito, M. Omura, J. A. Ketterling, S. Hirata, K. Yoshida, and T. Yamaguchi, Jpn. J. Appl. Phys. **61**, SG1049 (2022).
12) T. Oguri, M. Omura, W. Saito, K. Yoshida, and T. Yamaguchi, Jpn. J. Appl. Phys. **60**, SDDE24 (2021).
13) T. Mizoguchi, K. Yoshida, J. Mamou, J. Ketterling, and T. Yamaguchi, Jpn. J. Appl. Phys. **59**, SKKE17 (2020).
14) M. Omura, K. Yoshida, S. Akita, and T. Yamaguchi, J. Med. Ultrason. **47** [1], 25 (2020).
15) S. C. Lin, E. Heba, T. Wolfson, B. Ang, A. Gamst, A. Han, J. W. Erdman, W. D. O'Brien, M. P. Andre, C. B. Sirlin, and R. Loomaba, Physiology and behavior **176** [1], 139 (2016).
16) D. Ito, T. Oguri, N. Kamiyama, S. Hirata, K. Yoshida, and T. Yamaguchi, Jpn. J. Appl. Phys. **60**, SDDE11 (2021).
17) K. Osato, T. Oguri, N. Kamiyama, S. Hirata, K. Yoshida, and T. Yamaguchi, Jpn. J.

Appl. Phys. **62**, SJ1054 (2023).
18) M. Minagawa, H. Hasegawa, T. Yamaguchi, and S. Yagi, Jpn. J. Appl. Phys. **57**, 07LE07 (2018).
19) S. Fujii, M. Yamakawa, K. Kondo, T. Namita, and T. Shiina, Jpn. J. Appl. Phys. **58**, SGGE07 (2019).
20) I. Sporea, S. Bota, M. Peck-Radosavljevic, R. Sirli, H. Tanaka, H. Iijima, R. Badea, M. Lupsor, C. Fierbinteanu-Braticevici, A. Petrisor, H. Saito, H. Ebinuma, M. Friedrich-Rust, C. Sarrazin, H. Takahashi, N. Ono, F. Piscaglia, A. Borghi, M. D'Onofrio, A. Gallotti, A. Ferlitsch, A. Popescu, and M. Danila, European Journal of Radiology **81** [12], 4112 (2012).
21) J. E. Brandenburg, S. F. Eby, P. Song, H. Zhao, J. S. Brault, S. Chen, and K. An, Archives of Physical Medicine and Rehabilitation **95** [11], 2207 (2014).
22) E. Franceschini, and R. Guillermin, J. Acoust. Soc. Am. **132** [6], 3735 (2012).
23) E. Franceschini, R. Monchy, and J. Mamou, IEEE Trans. Ultrason. Ferroelectr. Freq. Control **63** [9], 1321 (2016).
24) G. Ghoshal, R. J. Lavarello, J. P. Kemmerer, R. J. Miller, and M. L. Oelze, Ultrasound Med. Biol. **38** [12], 2238 (2012).
25) Z. F. Lu, J. A. Zagzebski, and F. T. Lee, Ultrasound Med. Biol. **25** [7], 1047 (1999)
26) E. Saegusa-Beecroft, J. Machi, J. Mamou, M. Hata, A. Coron, E. T. Yanagihara, T. Yamaguchi, M. L. Oelze, P. Laugier, and E. Feleppa, J Surg Res. **183** [1], 258 (2013).
27) K. Tamura, J. Mamou, A. Coron, K. Yoshida, E. J. Feleppa, and T. Yamaguchi, IEEE Trans. Ultrason. Ferroelectr. Freq. Control **64** [10], 1501 (2017).
28) M. Omura, K. Yoshida, S. Akita, T. Yamaguchi, Jpn. J. Appl. Phys. **59**, SKKE15 (2020).
29) R. J. Lavarello, W. R. Ridgway, S. Sarwate, and M. L. Oelze, Ultrasound Med. Biol. **61** [6], 515 (2015).
30) M. L. Oelze, J. Mamou, IEEE Trans. Ultrason. Ferroelectr. Freq. Control **63** [2], 336 (2016).
31) K. Lee, J. Acoust. Soc. Am. **145** [5], EL393 (2019).
32) M. McCormick, E. Madsen, M. Deaner, and T. Varghese, J. Acoust. Soc. Am. **130** [2], 737 (2011).
33) B. Raju, and M. Srinivasan, Ultrasound Med. Biol. **27** [11], 1543 (2001).
34) M. Herd, T. Hall, J. Jiang, and J. Zagzebski, Ultrasound Med. Biol. **23** [1], 1 (2012).
35) M. Omura, R. Nagaoka, K.Yagi, K. Yoshida, T. Yamaguchi, and H. Hasegawa, Jpn.

J. Appl. Phys. **61**, SG1067 (2022).

36) M. Omura, H. Hasegawa, R. Nagaoka, K. Yoshida, and T. Yamaguchi, J. Med. Ultrason. **47** [1], 35 (2020).

37) E. Franceschini, R. Guillermin, and F. Tourniaire, J. Acoust. Soc. Am. **135** [6], 3620 (2014).

38) H. Kutsuzawa, S. Hirata, K. Yoshida, E. Franceschini, and T. Yamaguchi, Proc. Symp. Ultrason. Electron2023.

39) R. Kuc, M. Schwartz, IEEE Trans. Sonics Ultrason. **25** [5], 353 (1979).

40) N. Suzuki, in *Chouonnpabinran* (Handbook of Ultrasound), ed. Ultrasound Handbook Editorial Committee (Maruzen, Tokyo, 1999) pp421-422 [in Japanese].

41) L. Yao, J. Zagzebski, and E. Madsen, Ultrason. Imaging **12** [1], 58 (1990).

42) M. Oelze, W. D. O'Brien, J. Acoust. Soc. Am. **111** [5], 2308 (2002).

43) J. J. Faran, J. Acoust. Soc. Am. **23**, 405 (1951).

Figure Captions

Fig. 1. (Color Online) B-mode images of (a-1)-(c-1) phantom A and (a-2)-(c-2) phantom B acquired with (a) transducer I, (b) transducer II, and (c) linear array probe

Fig. 2. (Color Online) Amplitude envelopes of phantom A and B acquired using (a) transducer I, (b) transducer II, and (c) linear array probe

Fig. 3. (Color Online) Power spectrums of phantom A and B acquired using (a) transducer I, (b) transducer II, and (c) linear array probe

Fig. 4. (Color Online) Backscatter coefficients of phantom A and B acquired using (a) transducer I, (b) transducer II, and (c) linear array probe and theoretical values

Fig. 5. (Color Online) B-mode images of (a-1)-(c-1) phantom C, (a-2)-(c-2) phantom D and (a-3)-(c-3) phantom E acquired with (a) transducer I, (b) transducer II, and (c) linear array probe

Fig. 6. (Color Online) Amplitude envelopes of phantom A, B, C, D and E acquired using (a) transducer I, (b) transducer II, and (c) linear array probe

Fig. 7. (Color Online) Power spectrums of phantom A, B, C, D and E acquired using (a) transducer I, (b) transducer II, and (c) linear array probe

Fig. 8. (Color Online) Backscatter coefficients of phantom A, B, C, D and E acquired using

(a) transducer I, (b) transducer II, and (c) linear array probe and theoretical values

Fig. 9. (Color Online) Deviation between the estimated backscatter coefficients for phantom B, C, D, and E and the theoretical values calculated by the mathematical model

Fig. 10. (Color Online) B-mode images of (a-1)-(c-1) phantom D, (a-2)-(c-2) phantom F and (a-3)-(c-3) phantom G acquired with (a) transducer I, (b) transducer II, and (c) linear array probe

Fig. 11. (Color Online) Amplitude envelopes of phantom A, B, D, F and G acquired using (a) transducer I, (b) transducer II, and (c) linear array probe

Fig. 12. (Color Online) Power spectrums of phantom A, B, D, F and G acquired using (a) transducer I, (b) transducer II, and (c) linear array probe

Fig. 13. (Color Online) Backscatter coefficients of phantom A, B, D, F and G acquired using (a) transducer I, (b) transducer II, and (c) linear array probe and theoretical values

Fig. 14. (Color Online) Deviation between the estimated backscatter coefficients for phantom B, D, F, and G and the theoretical values calculated by the mathematical model

Table Ⅰ. Phantom composition and acoustic properties

Phantom	A	B	C	D	E	F	G
Volume fraction of scatter 1 [%]	0.5	-	0.5	0.5	0.5	2	5
Volume fraction of scatter 2 [%]	-	0.3	0.1	0.3	0.5	0.3	0.3

Scatterer 1: nylon with diameter of 5 μm, scatterer 2: acrylic with diameter of 20 μm.

Table Ⅱ. PSF near focus for each sensor

	Axial [μm]	Lateral [μm]
V327	109	300
PT35	42	95
L39-21gD	80	120

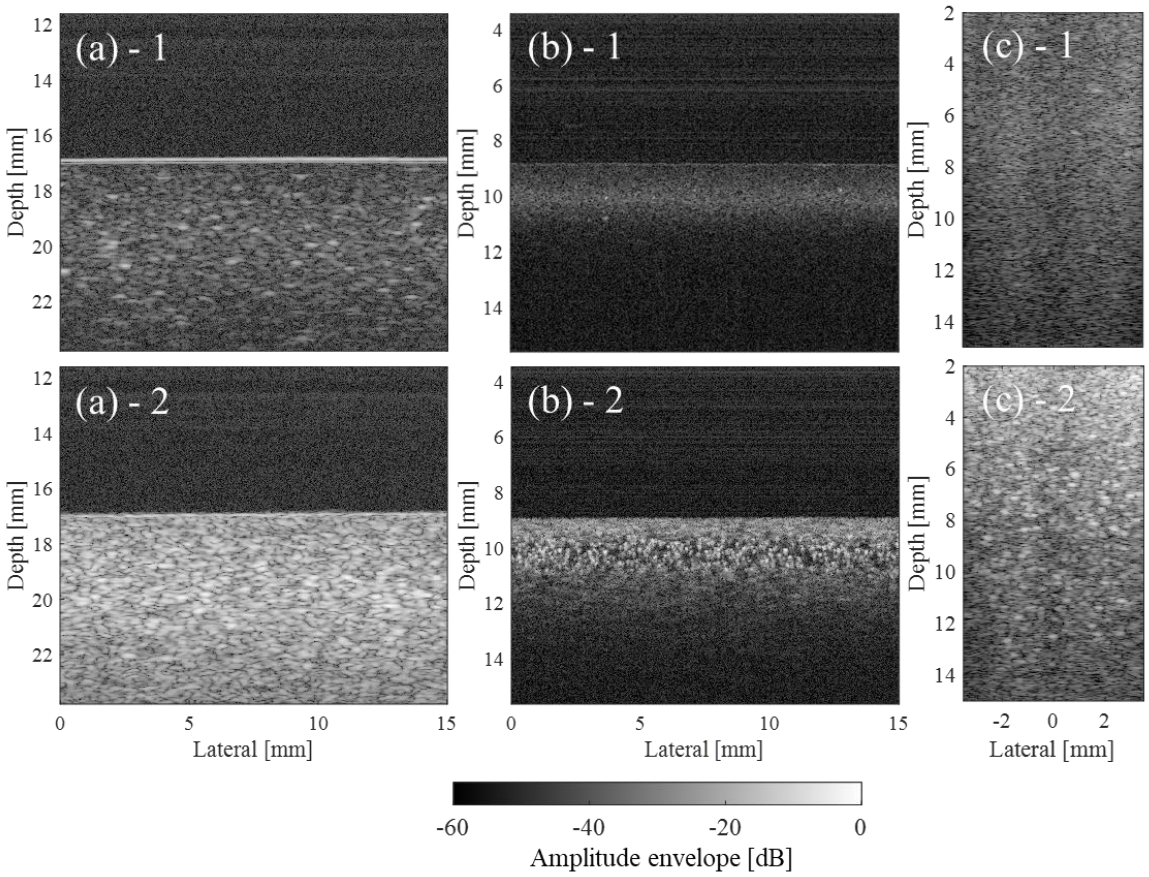
(a) - 1
(b) - 1
(c) - 1
(a) - 2
(b) - 2
(c) - 2
Depth [mm]
Lateral [mm]
-60
-40
-20
0
Amplitude envelope [dB]

Fig. 1

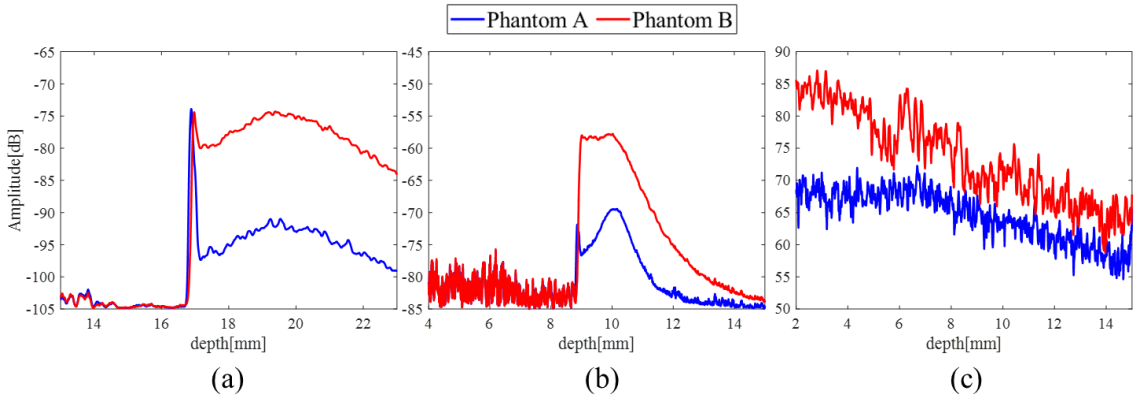
Phantom A
Phantom B
Amplitude[dB]
depth[mm]
(a)
(b)
(c)

Fig. 2

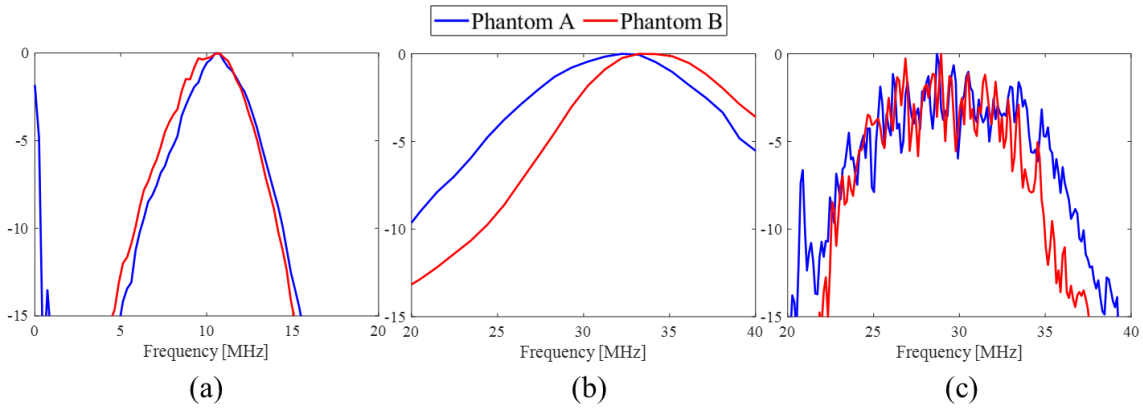
Phantom A
Phantom B
Frequency [MHz]
Frequency [MHz]
Frequency [MHz]
(a)
(b)
(c)

Fig. 3

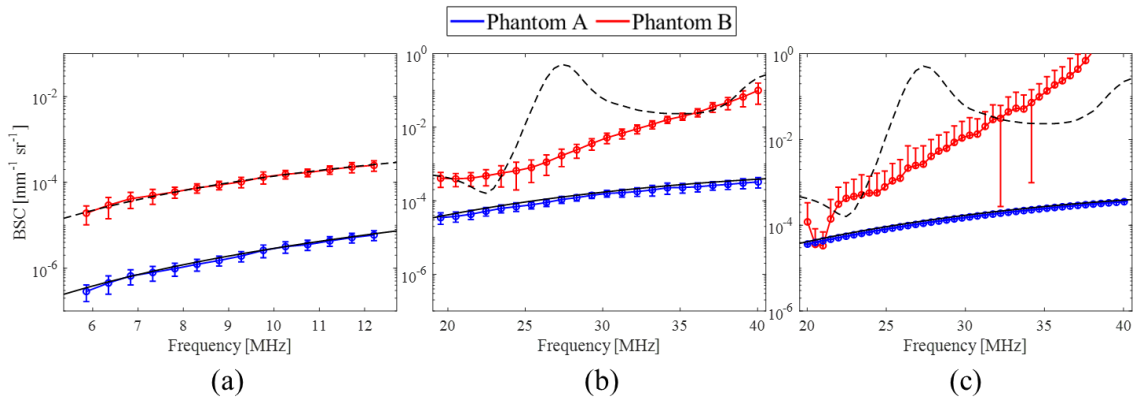
Phantom A
Phantom B
BSC [mm^{-1} sr^{-1}]
Frequency [MHz]
Frequency [MHz]
Frequency [MHz]
(a)
(b)
(c)

Fig. 4

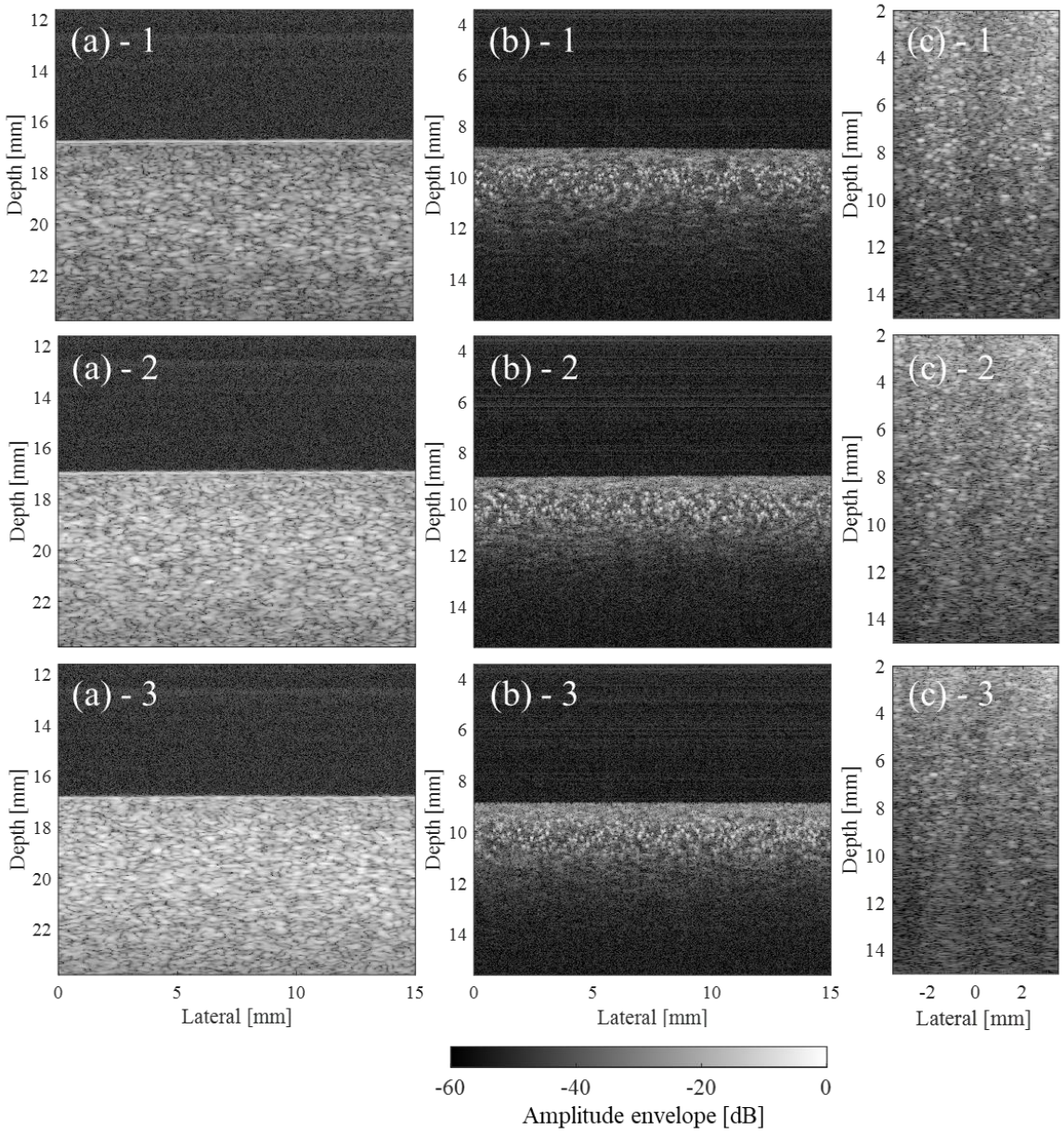
(a) - 1
(b) - 1
(c) - 1
(a) - 2
(b) - 2
(c) - 2
(a) - 3
(b) - 3
(c) - 3
Depth [mm]
Lateral [mm]
-60
-40
-20
0
Amplitude envelope [dB]

Fig. 5

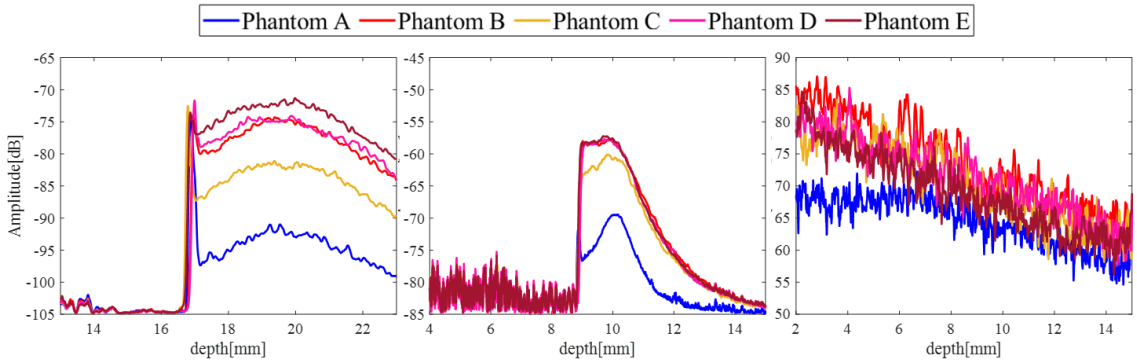

Fig. 6

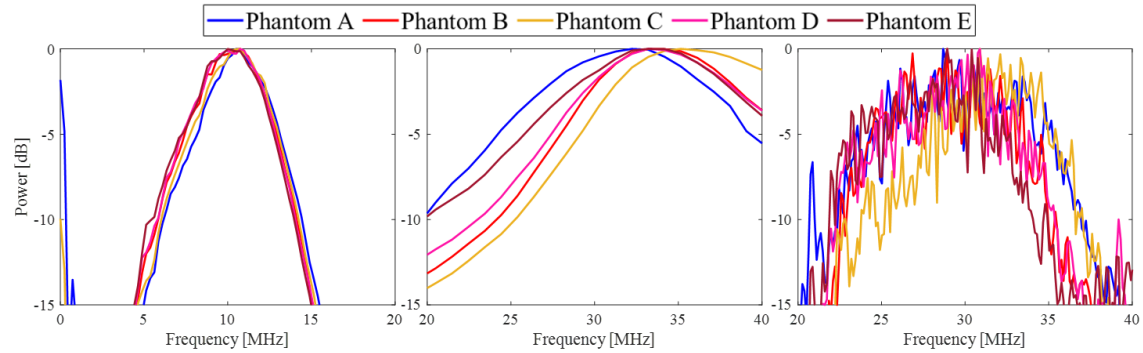

Fig. 7

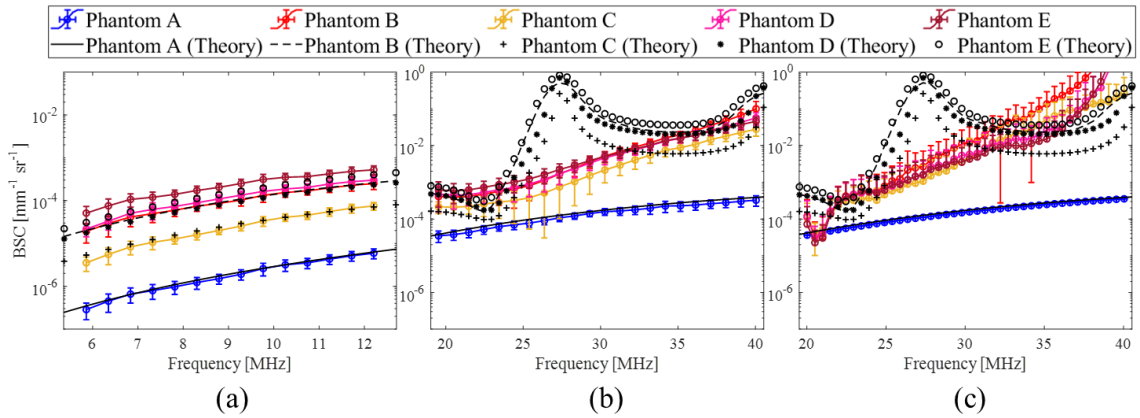

Fig. 8

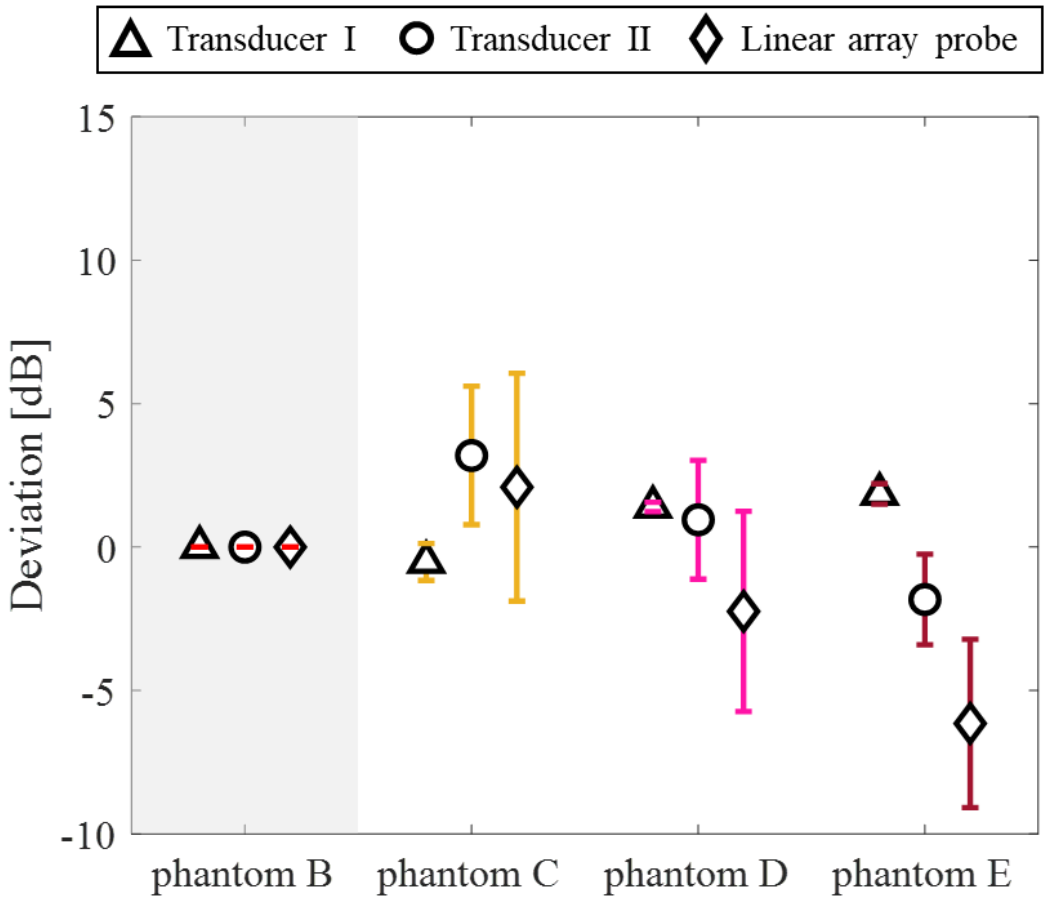
Transducer I
Transducer II
Linear array probe
15
10
5
0
-5
-10
Deviation [dB]
phantom B
phantom C
phantom D
phantom E

Fig. 9

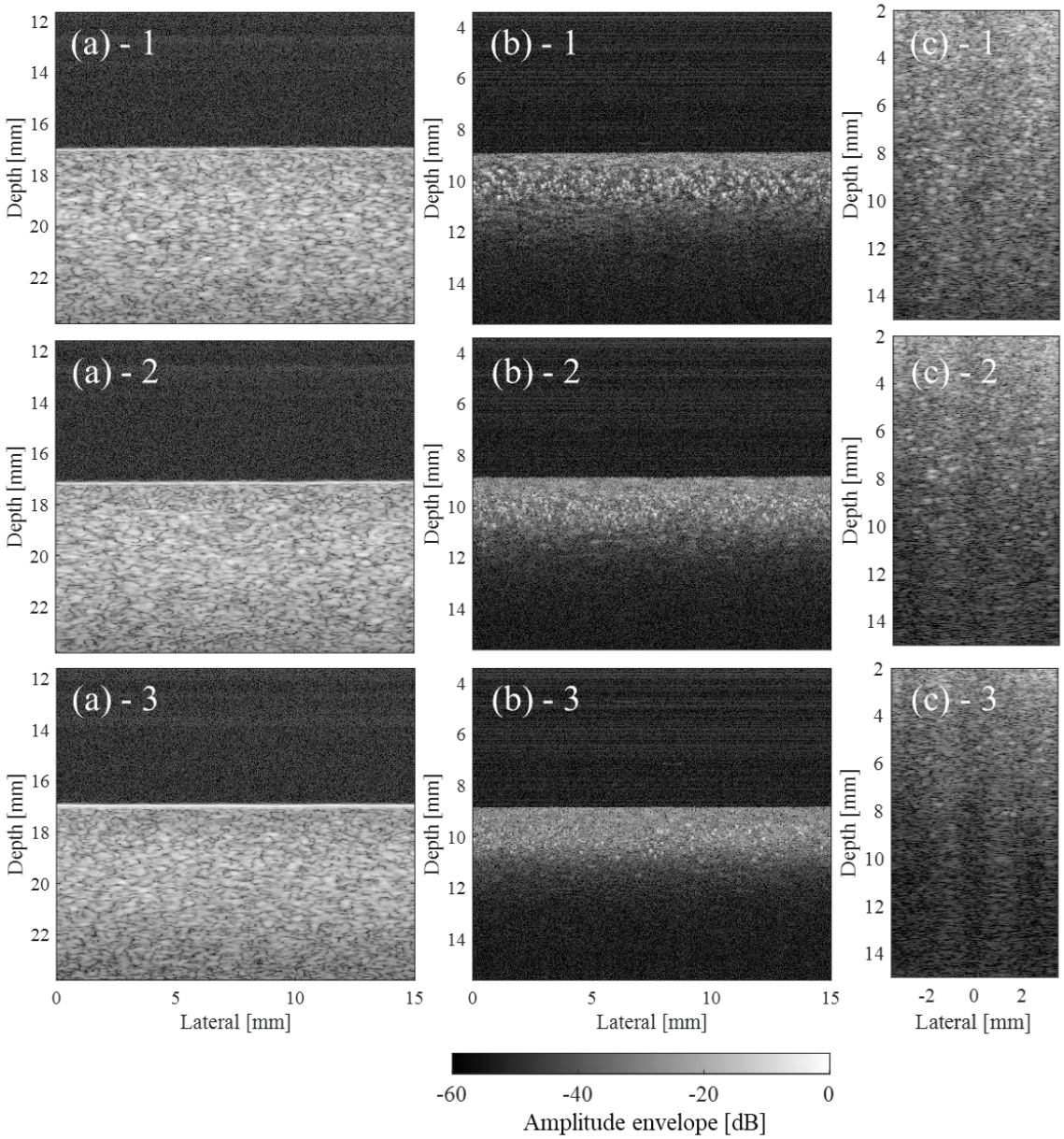
(a) - 1
(b) - 1
(c) - 1
(a) - 2
(b) - 2
(c) - 2
(a) - 3
(b) - 3
(c) - 3
Depth [mm]
Lateral [mm]
-60
-40
-20
0
Amplitude envelope [dB]

Fig. 10

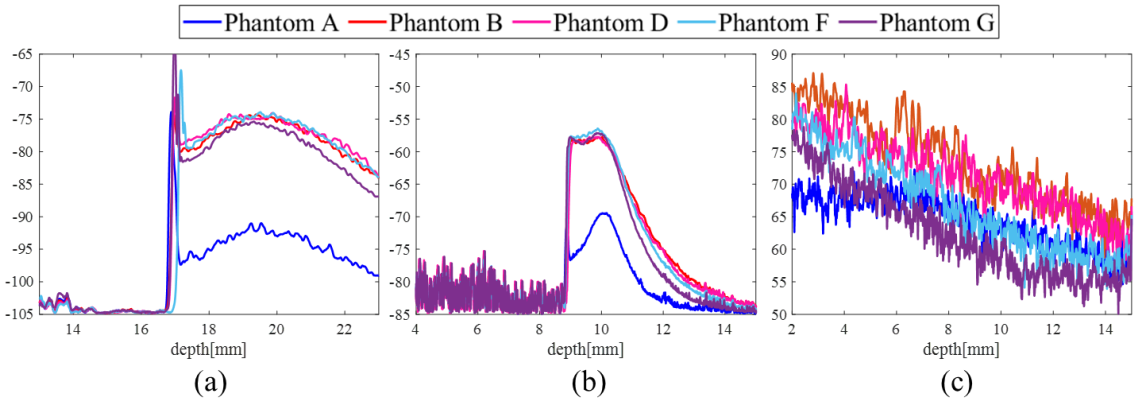

Fig. 11

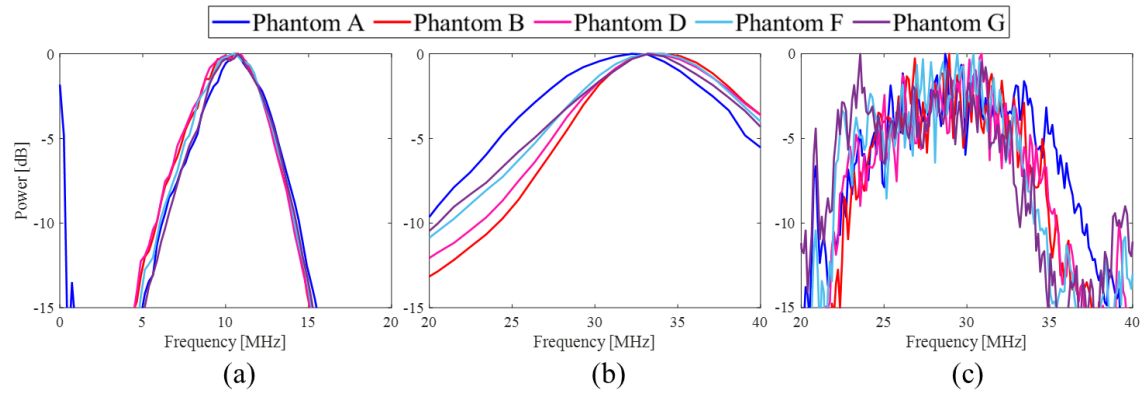

Fig. 12

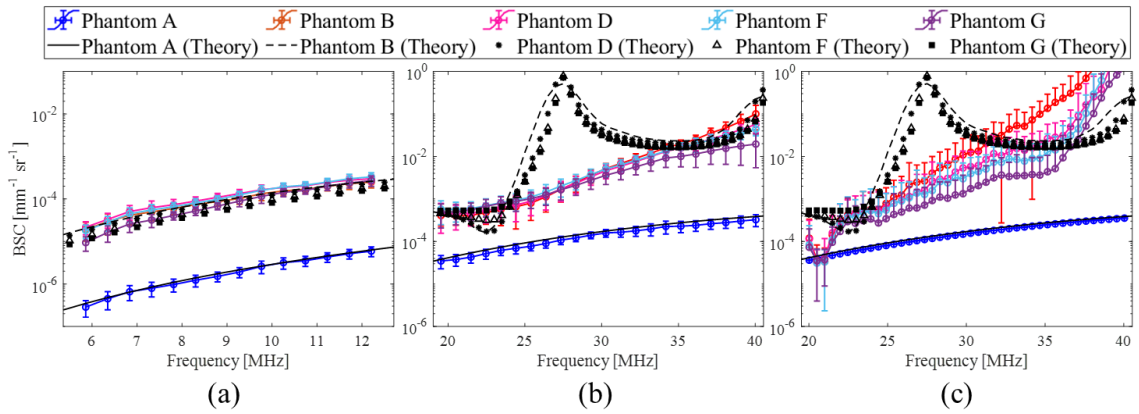

Fig. 13

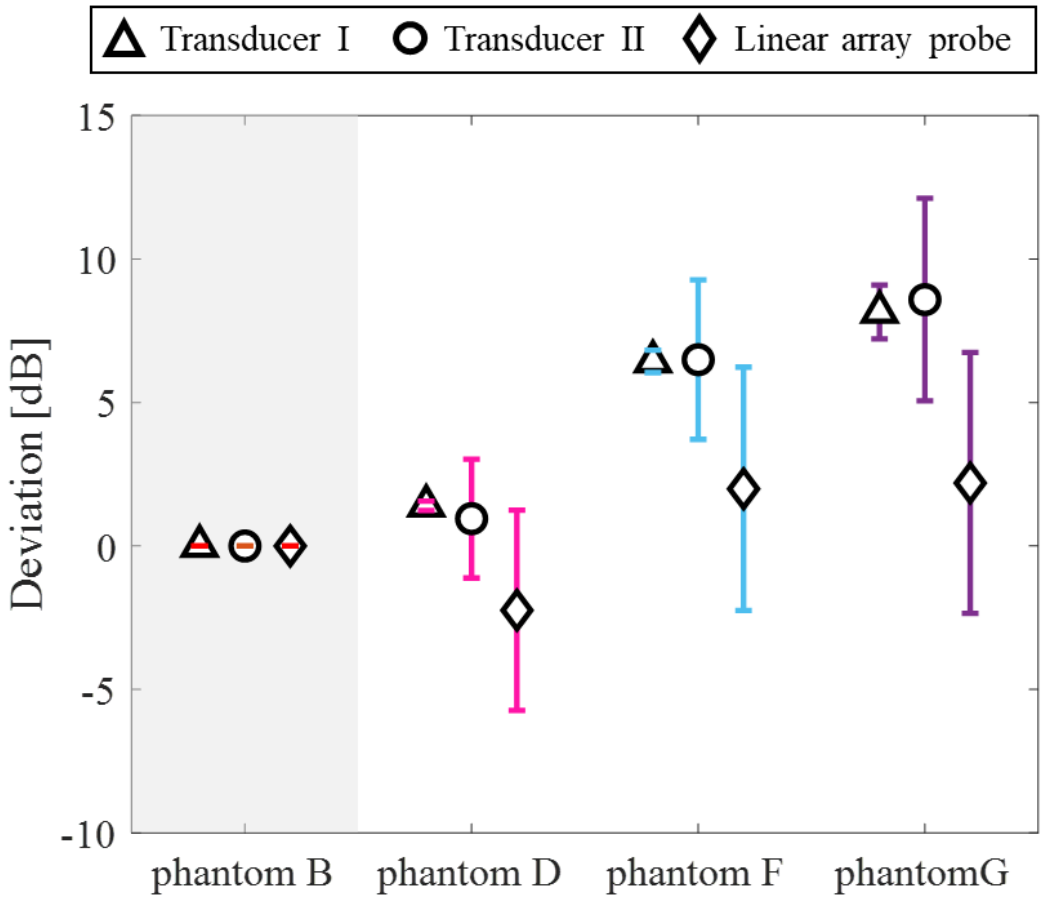
Transducer I
Transducer II
Linear array probe
Deviation [dB]
15
10
5
0
-5
-10
phantom B
phantom D
phantom F
phantomG

Fig.14